

SCIENTIFIC REPORTS



OPEN

Mapping of Low-Frequency Raman Modes in CVD-Grown Transition Metal Dichalcogenides: Layer Number, Stacking Orientation and Resonant Effects

Received: 11 August 2015
Accepted: 09 December 2015
Published: 14 January 2016

Maria O'Brien^{1,2,*}, Niall McEvoy^{1,2,*}, Damien Hanlon^{2,3}, Toby Hallam^{2,3}, Jonathan N. Coleman^{2,3} & Georg S. Duesberg^{1,2}

Layered inorganic materials, such as the transition metal dichalcogenides (TMDs), have attracted much attention due to their exceptional electronic and optical properties. Reliable synthesis and characterization of these materials must be developed if these properties are to be exploited. Herein, we present low-frequency Raman analysis of MoS₂, MoSe₂, WSe₂ and WS₂ grown by chemical vapour deposition (CVD). Raman spectra are acquired over large areas allowing changes in the position and intensity of the shear and layer-breathing modes to be visualized in maps. This allows detailed characterization of mono- and few-layered TMDs which is complementary to well-established (high-frequency) Raman and photoluminescence spectroscopy. This study presents a major stepping stone in fundamental understanding of layered materials as mapping the low-frequency modes allows the quality, symmetry, stacking configuration and layer number of 2D materials to be probed over large areas. In addition, we report on anomalous resonance effects in the low-frequency region of the WS₂ Raman spectrum.

Transition metal dichalcogenides (TMDs), such as MoS₂ and MoSe₂, have recently attracted significant attention from both industry and academia due to their wide range of fascinating properties^{1–3}. Unlike graphene, these materials possess a sizable bandgap and many reports indicate that they could be suitable as active layers in logic electronics and optoelectronics^{3–6} and as constituents in a variety of energy related applications^{7–10}. High-quality monolayer flakes of TMDs have previously been obtained via mechanical exfoliation^{1–3}; however, this method is serendipitous and suffers from low-throughput. Chemical¹¹ and liquid-phase exfoliation^{12–15} have greatly improved the prospect of scalability, however, the crystals produced by these methods typically have relatively small lateral dimensions rendering them ill-suited for many electronic applications. Large-scale TMD films have been obtained by sulfurization of metal oxide^{16,17} or metal films^{18–20}, but, the thus derived films are typically polycrystalline. Recently, there have been significant advances using chemical vapour deposition (CVD)^{21–28} to produce large-area, high-quality crystals, which could facilitate the realization of industry-relevant devices. In the case of each of these aforementioned synthesis routes it is imperative that the composition, quality and thickness of the materials produced is assessed before they can be considered for use in applications. Techniques such as atomic force microscopy and transmission electron microscopy are useful in the characterization of layer number and crystalline quality, respectively, but suffer from low sample throughput and laborious sample preparation.

Raman spectroscopy is a widely used technique in materials science and can be used to study molecular vibrations in 2D materials, which can reveal a wealth of information about material properties in a fast and non-destructive manner. In the case of graphene, Raman spectroscopy can be used to investigate the number

¹School of Chemistry, Trinity College Dublin, Dublin 2, Ireland. ²Centre for Research on Adaptive Nanostructures and Nanodevices (CRANN) and Advanced Materials and BioEngineering Research (AMBER) Centre, Trinity College Dublin, Dublin 2, Ireland. ³School of Physics, Trinity College Dublin, Dublin 2, Ireland. *These authors contributed equally to this work. Correspondence and requests for materials should be addressed to N.M. (email: nmcevoy@tcd.ie) or G.S.D. (email: duesberg@tcd.ie)

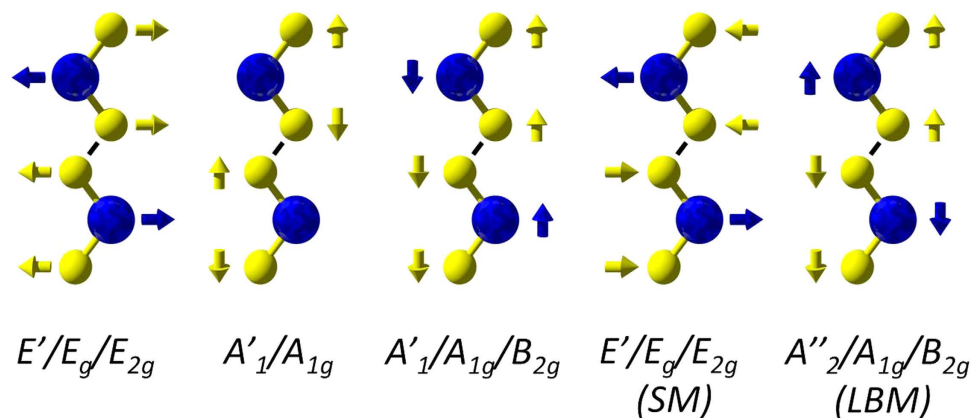


Figure 1. Schematic representation (ball and stick model) of Raman active modes in TMDs with the relative odd/even/bulk symmetry label indicated for each mode. Blue balls represent transition metal atoms; yellow balls represent chalcogen atoms, with arrows showing direction of motion.

and relative orientation of individual atomic layers, and can provide information on defect levels, strain and doping²⁹. Recent studies have shown that analogous information can be obtained for TMD samples, with each TMD having a characteristic spectrum. MoS₂ is the most heavily studied TMD to date and numerous reports on its Raman characteristics, and their dependence on layer number, have emerged. The most commonly reported Raman characteristics are those corresponding to reasonably large energy shifts, such as the in-plane E'_{2g} and the out-of-plane A_{1g} mode, which are observed at ~ 385 and ~ 405 cm^{-1} , respectively. Additional modes can be observed in the low-frequency (< 50 cm^{-1}) region of the Raman spectrum of TMDs, known as the shear modes (SMs) and layer-breathing modes (LBMs) and recent reports have demonstrated the practicality of studying these modes³⁰. These low-frequency modes occur due to relative motions of the planes themselves, either perpendicular or parallel to the atomic layers, and can prove useful in the characterization of 2D materials.

Herein, we present a systematic study of the low-frequency Raman peak positions and intensities of CVD-grown TMDs, including MoS₂, MoSe₂, WSe₂ and WS₂. These peaks were mapped out over large areas in regions consisting of crystals with different layer thickness, as are often found in CVD-grown samples, demonstrating the feasibility of using low-frequency Raman mapping for assessing layer number in TMD crystals. The same areas were also characterized using standard (high-frequency) Raman spectroscopy and photoluminescence (PL) spectroscopy. We identify different stacking configurations in MoSe₂ and WSe₂ by detailed analysis of Raman spectra and maps. Lastly, a newly observed resonant Raman mode, related to the $LA(M)$ mode, has also been identified in the low-frequency region of the WS₂ Raman spectrum.

Results and Discussion

TMDs can exist in 3 polytypes, depending on the co-ordination of chalcogen atoms around the metal atoms, and the stacking order of the layers. The first, 1T, is a metallic crystal with octahedral co-ordination that has recently been artificially synthesized for device applications³¹. However, since this polytype is metastable and not found in nature³², we will not discuss it here. The more common 2H and 3R polytypes are semiconducting, with trigonal prismatic coordination, with similar properties but differing stacking orders of metallic and chalcogen atoms. For example, 2H has a stacking order of AbA BaB AbA BaB, where capital letters indicate chalcogen atoms and lower-case letters indicate metal atoms, while 3R has a typical stacking order of AbA BcB CaC AbA, or the inverted AbA CaC BcB AbA³². The layers can also adopt a mixture of these stacking configurations, whereby, for example in a 3L sample, layers 1–2 obey 2H stacking, and layers 2–3 obey 3R stacking³³. This means that a 3L 2H-3R sample could have the stacking configuration AbA BaB CbC, or AbA BaB AcA. The properties of 2H and 3R TMDs have been reported to be almost identical³², with little observable change in the high-frequency region of the Raman spectrum. However, recent reports indicate slight differences in band structures and absorption spectra between the two stacking types^{34,35}. This shows that further investigation into the identification and properties of these stacking configurations is important both for fundamental studies of these materials and for future studies in the emerging field of van der Waals heterostructures³⁶ where the stacking order of two dissimilar layers could change the electronic and optical properties^{37,38} of artificial³⁹ or grown⁴⁰ heterostacks. In this study, we refer to 2H stacked crystals unless explicitly stated otherwise.

The Raman spectra of 2H and 3R semiconducting TMDs generally display two main characteristic vibrational modes. These are the $E'/E_g/E'_{2g}$ and A'_1/A_{1g} first-order modes at the Brillouin zone centre, shown in Fig. 1, that result from the in-plane and out-of-plane vibrations, respectively, of metal (M) and chalcogen (X) atoms^{41–43}. Different peak labels are used for different layer numbers due to the changing symmetry of the point group from D_{3h} (odd layer number) to D_{3d} (even layer number) to D_{6h} (bulk). These Raman active modes have been shown to shift in position with number of layers^{26,44–46}, allowing mono- and few-layer crystals to be identified. For example, in the case of MoS₂, as the layer number increases, interlayer van der Waals (vdW) forces suppress atomic vibrations meaning higher force constants are observed⁴⁴. This means that the out-of-plane A'_1/A_{1g} mode becomes blue-shifted at higher layer numbers (~ 2 cm^{-1} from monolayer to bilayer), as the vibrations of this mode are more strongly affected by vdW forces between the layers. The in-plane $E'/E_g/E'_{2g}$ mode in contrast shows a red

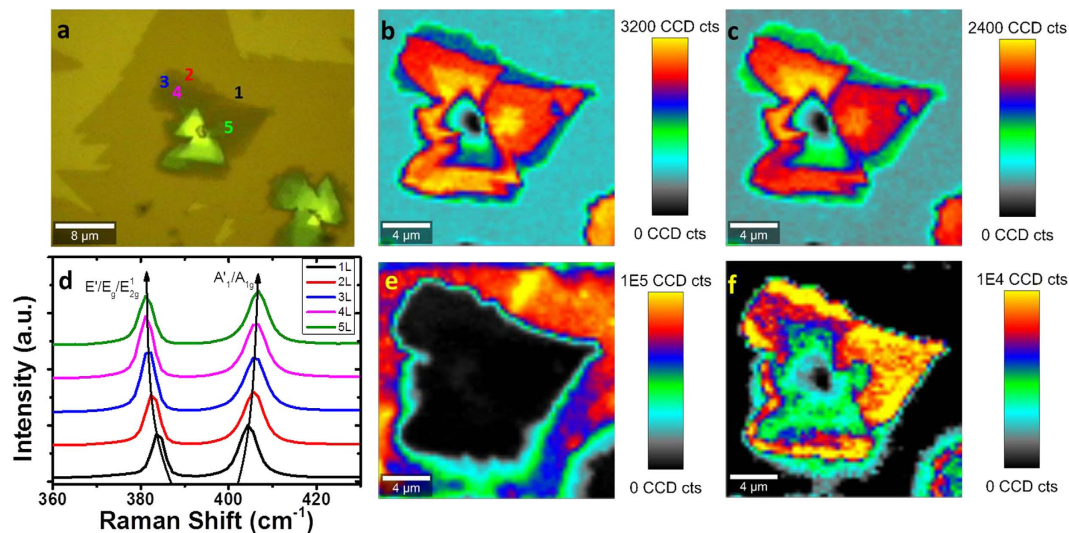


Figure 2. (a) Optical image of CVD MoS₂ with layer numbers labelled. (b) Peak intensity map of A₁/A_{1g} (~403 cm⁻¹) high-frequency Raman mode. (c) Peak intensity map of E'_g/E'_{2g} (~385 cm⁻¹) Raman mode. (d) Raman spectra of 1–5L MoS₂. (e) Peak intensity map of A1 exciton PL peak. (f) Peak intensity map of B1 exciton PL peak.

shift as layer number increases (~2 cm⁻¹ from monolayer to bilayer). This is attributed to structural changes in the material or to an increase in long-range Coulombic interlayer interactions affecting the atomic vibrations^{30,44}. However, for the transition metal diselenides, such as MoSe₂ and WSe₂, these changes in frequency for different layer numbers are not as dramatic (e.g. a shift of ~1 cm⁻¹ in the A_{1g} peak from 2 to 3L MoSe₂)^{45,47}, and may be below the instrumental spectral resolution of standard equipment. Furthermore, crystallite size⁴⁸, doping and strain have been shown to significantly alter the Raman spectra of TMDs. Previous reports have shown a red shift and broadening of the A₁/A_{1g} peak in MoS₂ with n-doping⁴⁹ and a blue shift and enhancement of the A₁/A_{1g} peak with p-doping⁵⁰. The Raman spectrum of MoS₂ is also highly sensitive to strain with the application of uniaxial strain resulting in the degeneracy of the E'_g/E'_{2g} mode being lifted⁵¹, whereas the introduction of localized wrinkles and folds has been shown to cause a red shift of both A₁/A_{1g} and E'_g/E'_{2g} modes⁵². Given the large number of factors that can affect the primary peaks in the Raman spectra of TMDs, an alternative method for the clear assessment of TMD layer numbers using Raman spectroscopy is desirable.

Investigation of the low-frequency SM and LBM has been suggested as a universal method of layer number (N) determination in TMD materials³⁰, due to the fact that the layer-breathing mode vibrations are themselves out of plane and vary significantly as a function of layer number. The relative atomistic motions of the SMs and LBMs in TMDs are illustrated in Fig. 1, whereby the SM involves the in-plane motion of metal and chalcogen atoms, and the LBM involves the out-of-plane motion of metal and chalcogen atoms⁴³. These SMs and LBMs are not present in single layers, but show a characteristic blue and red shift, respectively as layer number increases from 2L to bulk. While not commonly used as a metric for layer thickness in 2D materials currently, due their Raman shift position appearing in the ultra-low frequency region beyond the filter cut-offs for most commercial Raman spectrometers, ongoing developments in the use of components such as multiple notch filters⁵³ can allow measurement of these peaks with low excitation powers and short acquisition times. Full measurement and analysis of these modes is desirable for a more comprehensive understanding of the mechanical and electrical properties of TMDs⁵⁴.

The low-frequency SMs and LBMs have been extensively studied in graphene^{53,55} and have been reported for a number of mechanically exfoliated TMDs^{30,54,56}. Unlike graphene, which consists of single atomic layers of carbon, TMD monolayers consist of three atomic layers of chalcogen/metal/chalcogen, resulting in a richer and more complex Raman spectrum. While previous reports have outlined the evolution of low-frequency peak positions with layer number⁵⁷, this has not yet been comprehensively studied for all layered materials. In addition, recent reports have identified new peaks in the low-frequency region of MoSe₂ corresponding to different polytypes of the material, indicating that Raman shifts in this region are of interest for considering differences in interlayer interactions with stacking type³³. Here, by means of Raman mapping, we image the peak intensities and positions of SMs and LBMs for different TMDs and highlight the efficacy of this technique for layer-number identification. We further outline the effectiveness of this technique for quickly distinguishing between different stacking configurations which are prevalent in transition metal diselenide layers.

MoS₂ Raman Mapping

In Fig. 2(a), a sample of CVD-grown MoS₂ with multiple distinct layers present is shown. In MoS₂, the in-plane (E'_g/E'_{2g}) and out-of-plane (A₁/A_{1g}) peaks occur in the vicinity of ~385 and ~403 cm⁻¹, respectively. Figure 2(d) shows the evolution of Raman spectra (normalized to A₁/A_{1g} peak intensity) extracted from 1–5L MoS₂, which display a characteristic red and blue shift of the E'_g/E'_{2g} and A₁/A_{1g} modes, respectively as the layer number

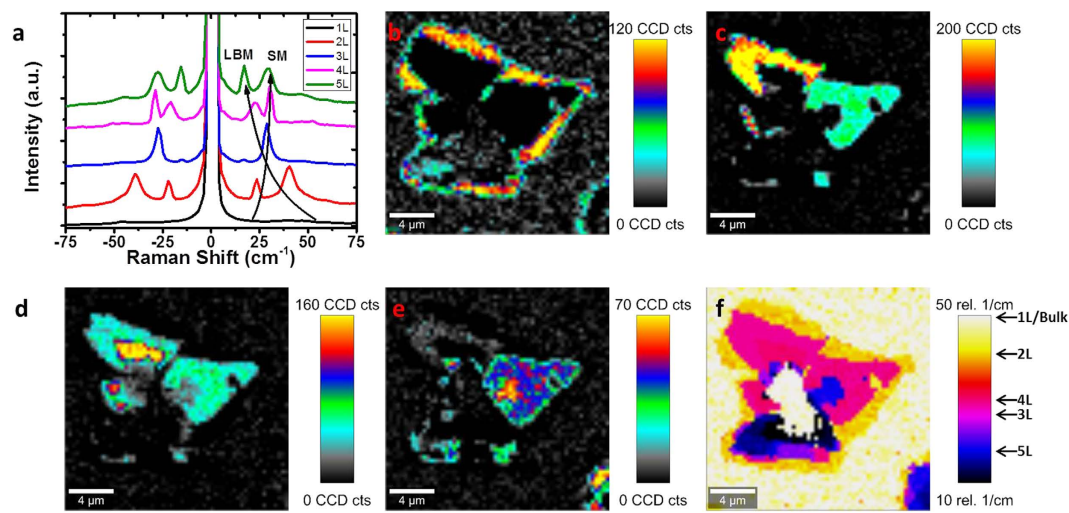


Figure 3. (a) Low-frequency Raman spectra of SMs and LBMs of 1, 2, 3, 4 and 5L MoS₂. (b) Peak intensity map of LBM mode for 2L MoS₂ at ~40 cm⁻¹. (c) Peak intensity map of max SM/LBM for 3L MoS₂ at ~29 cm⁻¹. (d) Peak intensity map of max SM for 4L MoS₂ at ~31 cm⁻¹. (e) Peak intensity map of LBM for 5L MoS₂ at ~17 cm⁻¹. (f) Map of position of maximum peak intensity in the region of 10–50 cm⁻¹.

increases^{44,46}. Peak intensity maps are presented in Fig. 2(b,c), showing an increase in intensity of A'_1/A_{1g} and $E'/E'_g/E^1_{2g}$ peaks as layer number increases from 1–5 layers, with a subsequent decrease as layer number increases towards bulk, attributed to optical interference occurring for the excitation laser and emitted Raman scattering⁴⁶. The peak position maps for A'_1/A_{1g} and $E'/E'_g/E^1_{2g}$ are shown in the supporting information, with Figure S1(a) and S1(b) showing clearly the red and blue shift in $E'/E'_g/E^1_{2g}$ and A'_1/A_{1g} peaks, respectively, as layer number increases, allowing an initial assessment of layer number to be made. This assessment is supported by PL intensity maps of the same area, shown in Fig. 2(e,f), showing a maximum intensity of A1 excitons in monolayer regions, and an enhancement of B1 exciton intensity in multilayer regions. The corresponding shift in PL position as layer number increases, reflecting the changing bandgap of MoS₂ with layer number, is illustrated in the peak position maps in Figure S1(d) and (e) in the supplementary information, and in the corresponding spectra in Figure S1(f).

Figure 3 presents the low-frequency SMs and LBMs of MoS₂. Spectra of 1–5L MoS₂ are shown in Fig. 3(a), in close agreement with previous measurements of mechanically exfoliated MoS₂^{30,54}. Figure 3(b–e) show peak intensity maps of SMs/LBMs for 2–5L MoS₂. There is some overlap in peak intensity maps, due to peaks for different layer numbers appearing at similar Raman shifts; however, the relative intensity of these modes provides a strong indication of layer number. While peak intensity maps allow a step-by-step assignment of layer number, this can be better visualized by generating a map of the position of maximum peak intensity in the low-frequency regime as shown in Fig. 3(f). Such mapping represents a clear and facile method of assigning the layer number present in MoS₂, by uniquely identifying the highest intensity SMs and LBMs present in 2–5L MoS₂ by their position in the range of 10–50 cm⁻¹, noting that 1L MoS₂ has no peaks in this region.

MoSe₂ Raman Mapping

Raman analysis of CVD-grown MoSe₂ with a variety of layer numbers is shown in Fig. 4. In MoSe₂, the in-plane ($E'/E'_g/E^1_{2g}$) and out-of-plane (A'_1/A_{1g}) Raman active modes occur in the vicinity of ~287 and ~240 cm⁻¹, respectively. The significant red shift of peaks compared with MoS₂ occurs due to the larger mass of the selenium vs. sulfur atoms⁵⁴. Similar to MoS₂, the in-plane ($E'/E'_g/E^1_{2g}$) and out-of-plane (A'_1/A_{1g}) modes exhibit a red and blue shift, respectively, with increasing layer thickness. In Fig. 4(a), an optical image of CVD grown layers is shown. A Raman map of A'_1/A_{1g} (~240 cm⁻¹) peak intensity is shown in Fig. 4(b), with the corresponding peak position map in Figure S2(a) in the supporting information. It is clear from these images that while the intensity varies significantly with thickness, following an initial jump from 1 to 2L, the A'_1/A_{1g} (~240 cm⁻¹) position does not change dramatically with layer number. A map of the $E'/E'_g/E^1_{2g}$ (~287 cm⁻¹) intensity is shown in Fig. 4(c), with the corresponding position map in Figure S2(b) in the supporting information. This Raman mode's intensity and position changes significantly from monolayer to bilayer, but shows no further significant change between 2, 3, and 4 layers, and is therefore not useful for layer number determination. Figure 4(d) shows spectra of 1 to 4L 2H MoSe₂ crystals extracted from different areas in Fig. 4(a), which are in good agreement with previously reported spectra^{42,47,56}. We can also consider the intensity maximum and position maps of the $A'_1/A_{1g}/B^1_{2g}$ mode (~350 cm⁻¹). This mode is inactive in bulk material, but has previously been observed to become weakly Raman active in bilayer and few-layer crystals due to the breakdown of translation symmetry⁴². To avoid confusion with other modes, this will henceforth be referred to as the B^1_{2g} mode. As this mode does not appear for monolayer MoSe₂, as shown in the peak intensity map in Fig. 4(e), its absence (in combination with a characteristic PL signal) serves as a confirmation of monolayer presence. However, similar to $E'/E'_g/E^1_{2g}$ (~287 cm⁻¹), it does not shift significantly in intensity or position for 2+ layers as shown in the map of B^1_{2g} position in Figure S2(d) of the Supporting Information. A map of PL intensity is shown in Fig. 4(f), with the corresponding position map and

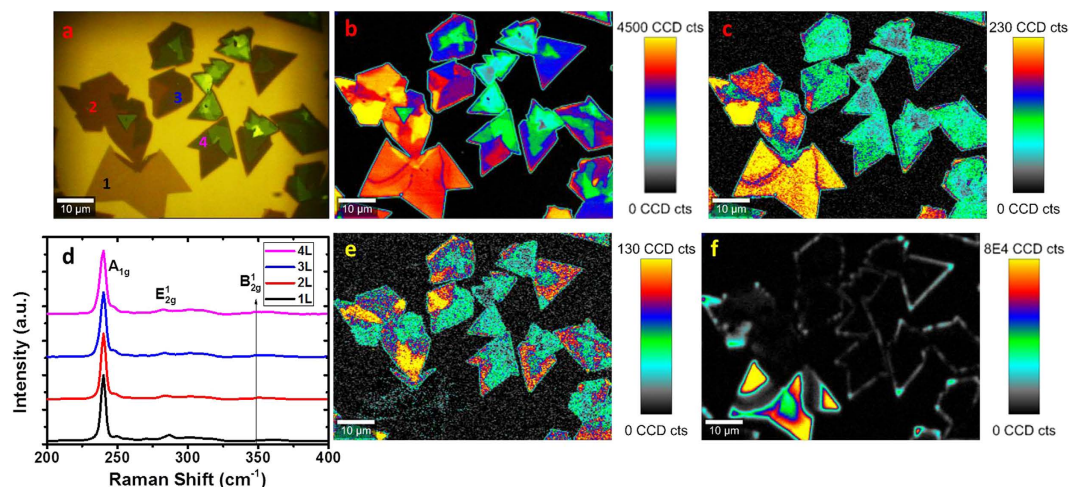


Figure 4. (a) Optical image of CVD-grown MoSe₂ with varying layer numbers. (b) Peak intensity map of A_1'/A_{1g} (~ 240 cm⁻¹) Raman mode for MoSe₂. (c) Peak intensity map of $E_1'/E_g/E_{12g}$ (~ 287 cm⁻¹) Raman mode. (d) Raman spectra of 1–5L MoSe₂ normalized to A_1'/A_{1g} mode intensity. (e) Peak intensity map of B_{12g} (~ 350 cm⁻¹) mode. (f) PL intensity map.

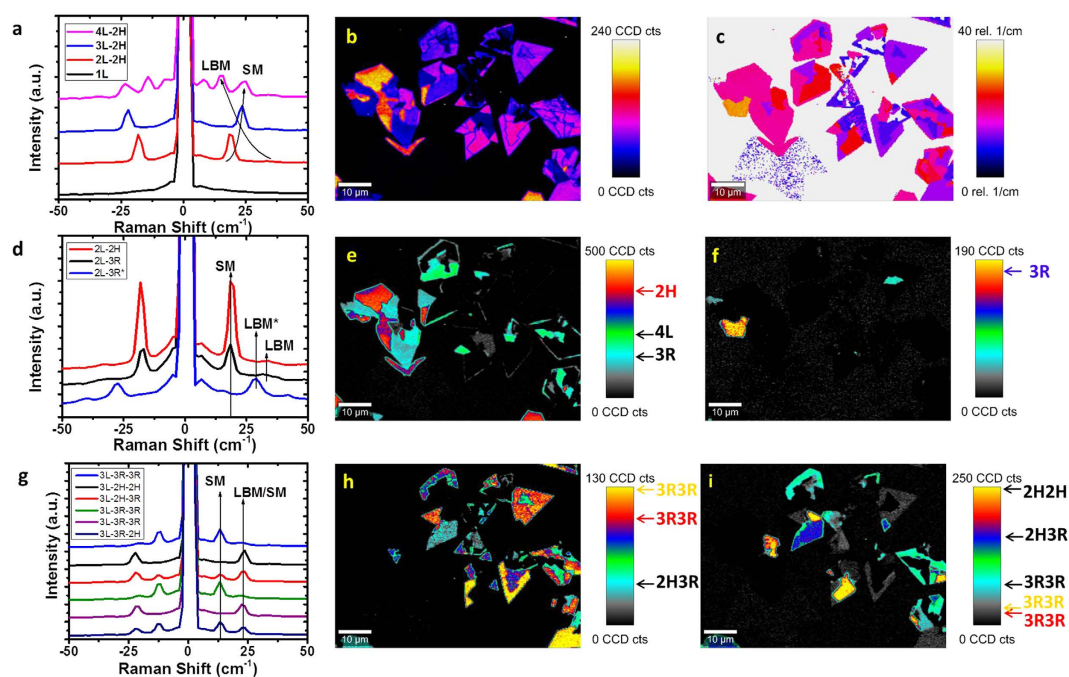


Figure 5. (a) Low-frequency Raman spectra of SMs and LBMs of 1, 2, 3, and 4L 2H MoSe₂. (b) Peak intensity map over the range 10–50 cm⁻¹. (c) Map of position of maximum peak intensity of the low-frequency Raman modes in the range of 0–40 cm⁻¹. (d) Low-frequency Raman spectra of SMs and LBMs of 2H and 3R stacking configurations in 2L MoSe₂. (e) Peak intensity map for 2L MoSe₂ SM at ~ 18 cm⁻¹. (f) Peak intensity map for 2L MoSe₂ LBM at ~ 29 cm⁻¹. (g) Enhanced low-frequency Raman spectra of SMs and LBMs of 2H and 3R combination stacking configurations for 3L MoSe₂. (h) Peak intensity map for 3L MoSe₂ at ~ 13 cm⁻¹. (i) Peak intensity map for 3L MoSe₂ at ~ 24 cm⁻¹.

spectra shown in Figure S2(e) and (f), respectively in the Supporting Information. The intense PL seen in certain areas serves as confirmation of monolayer presence, with some drop-off in intensity, as expected, in the regions of grain boundaries. The apparent lack of PL in other layers does not necessarily signify bulk behaviour – rather the signal for few-layer crystals is overshadowed by that of the monolayer.

We now focus on the study of low-frequency Raman modes in MoSe₂. Figure 5(a) shows spectra of 1 to 4L 2H-MoSe₂ which have been extracted from different areas marked in the optical image in Fig. 4(a), and are in close agreement with spectra previously shown in the literature⁴⁷. These spectra have been normalized to the intensity of the high-frequency A_{1g} mode, and offset for clarity, as have the rest of the MoSe₂ spectra in Fig. 5.

A Raman map of the maximum signal over the range 10–50 cm^{-1} is shown in Fig. 5(b). Interestingly, this map shows fractures and splitting in areas where no change is discernible in the optical image and therefore further investigation into the low-frequency modes was warranted. By analysis of various regions that appeared to be the same thickness according to optical contrast, it was possible to extract different low-frequency Raman signals correlating to different combinations of 2H and 3R stacking of MoSe_2 layers. These different stacking configurations have previously been observed in CVD-grown transition metal diselenide layers and their formation attributed to the small difference in formation energy between the two different configurations⁵⁸. It should be noted that there was no evidence of these different stacking configurations in our CVD-grown MoS_2 , with all areas probed displaying a purely 2H signal. In Fig. 5(c), a map of position of peak intensity maximum in the low-frequency region is shown. Study of the differences in intensity maximum in Fig. 5(b) and the position of this intensity maximum for each layer shows that there is no direct overlap in each – rather, some areas have peaks of maximum intensity in the same position but of different intensity, while others have peaks of similar intensity but in different areas. To explain this observation, we will examine the low-frequency spectra for each layer number. In Fig. 5(d), low-frequency Raman spectra for different regions of 2L MoS_2 are shown, corresponding to 2H (max at 18 cm^{-1}), 3R (max at 18 cm^{-1} , but significantly lower in relative intensity), and 3R* (max at 29 cm^{-1}). The difference between 3R (max at 18 cm^{-1}) and 3R* (max at 29 cm^{-1}) is attributed to one being 3R, and the other being the vertically flipped 3R³³, labelled as 3R* here, which would interact radically differently with incoming phonons. The intensity maximum for 2H and 3R (18 cm^{-1}) is shown in Fig. 5(e), which shows (with some overlap with peaks present in 4L) the areas where these peaks are present. The difference in intensity between 2H and 3R here is consistent with previous reports³³. Additionally, as shown in Fig. 5(f), we also observe experimentally for the first time a predicted Raman mode at $\sim 29 \text{ cm}^{-1}$, attributed to the A_1 mode in the 3R* stacking configuration³³. Similar evidence for different stacking configurations is seen in the 3L low-frequency Raman spectra in Fig. 5(g), where it is possible to identify a variety of 3L stacking configurations, including 2H-2H, 2H-3R, and 3R-3R. The trends in intensity for the peaks at $\sim 13 \text{ cm}^{-1}$ and $\sim 24 \text{ cm}^{-1}$ are clear when the peak intensity maps are considered. In Fig. 5(h), a peak intensity map of the SM at $\sim 13 \text{ cm}^{-1}$ is shown, which is present for 3R-3R stacking, but also present at higher intensities as the SM mode in 2H-3R stacking, where it appears in parallel with another SM mode at 24 cm^{-1} . Therefore, the relative intensity of this mode at $\sim 13 \text{ cm}^{-1}$ can be used to distinguish between 3R-3R and 2H-3R stacking, as labelled on the intensity scale bar in Fig. 5(h), with further verification of the 2H-3R mode afforded by the presence of a SM/LBM overlap peak at $\sim 24 \text{ cm}^{-1}$, the intensity of which is mapped out in Fig. 5(i). This peak is highest in intensity in 2H-2H stacking, as is expected for pristine mechanically exfoliated 2H crystals⁵⁶, and decreases as stacking configuration goes from 2H-2H to 2H-3R to 3R-3R. This is logical when considering the decreasing interlayer interactions and force constants present in 3R stacking in comparison to 2H stacking. The respective intensities for the different stacks, as shown in Fig. 5(i), indicate clearly that different intensities are present for this peak in different areas, allowing one to distinguish between 2H-2H, 2H-3R and different 3R-3R stacking configurations. The use of Raman intensity maps serves to highlight the ubiquitous nature of the different stacking configurations, which would not be readily apparent in comparing individual spectra of different crystals, or in the study of high-frequency point spectra, which show little change between 2H and 3R stacking configurations³², as shown in the extracted high-frequency spectra in Figure S4 and discussed in the Supporting Information. Low-frequency Raman mapping can distinguish between different stacking configurations rapidly and non-destructively, allowing TMDs in different stacking configurations to be identified and studied without the need for high-resolution imaging³⁹. The peak positions of SMs and LBMs observed here are in good agreement with previously observed low-frequency modes in mechanically exfoliated 2H MoSe_2 ^{56,60} and CVD-grown MoSe_2 stacking polytypes³³. Raman spectra of different stacking configurations for 4L MoSe_2 are shown in Figure S3 and discussed in the Supporting Information. Layer number assignments have been confirmed using atomic force microscopy (AFM) as detailed in the Supporting Information, Figures S5 and S6.

WSe₂ Raman Mapping

A sample of CVD-grown WSe_2 with a variety of layer numbers present is shown in Fig. 6(a). The WSe_2 Raman spectrum displays the in-plane (E'/E_g) and out-of-plane (A'_1/A_{1g}) modes typical for layered TMDs. Under the experimental conditions used here, these appear as a single overlapping peak at $\sim 250 \text{ cm}^{-1}$ in mono- and few-layer WSe_2 . In the case of resonant excitation conditions, as applies when using a 532 nm excitation laser in resonance with the A' exciton peak of WSe_2 ^{61,62}, the $2LA(M)$ phonon also appears. This is a second order resonant Raman mode that occurs due to LA phonons at the M point in the Brillouin zone⁴⁵, similar to the case of MoS_2 and WS_2 in resonance^{26,63,64}. Figure 6(d) shows spectra of 1 to 3L WSe_2 extracted from different areas marked in Fig. 6(a), which are in agreement with previous studies^{56,58}. A peak intensity Raman map of the peak at $\sim 250 \text{ cm}^{-1}$ is shown in Fig. 6(b), with the corresponding position map in Figure S7(a) in the Supporting Information. This peak is a combination of contributions from the A'_1/A_{1g} and $E'/E_g/E'_{2g}$ modes that coincidentally overlap at this Raman shift. This mode shows a decrease in intensity with layer number, and a slight shift in position as shown and discussed in Figure S7(a) in the Supporting Information. The changing intensity of this peak between the two bilayer regions, as labelled on the optical image, indicates some change in stacking configuration, with one region appearing at a higher intensity than the other⁵⁸. This is likely due to a decrease in in-plane contributions due to decreasing magnitudes of Raman tensors in 3R symmetry contributions, but high-frequency modes alone are not sufficient to assign a definitive stacking configuration to each region. The labels shown on the optical image will be discussed in the low-frequency analysis below. A Raman map of the $2LA(M)$ mode ($\sim 260 \text{ cm}^{-1}$) intensity is shown in Fig. 6(c), with the corresponding position map in Figure S7(b). The $2LA(M)$ mode's intensity changes significantly from monolayer to bilayer, but shows no further significant change for 3L. It is clear that this mode, similar to the peak at 250 cm^{-1} , is also more intense for one bilayer region than another. The relative intensity of $2LA(M)$ increases with respect to the A'_1/A_{1g} and $E'/E_g/E'_{2g}$ combination peak, however, the overall intensity decreases sufficiently for this not to be apparent in the peak intensity maps. The B_{2g} ($\sim 310 \text{ cm}^{-1}$) peak

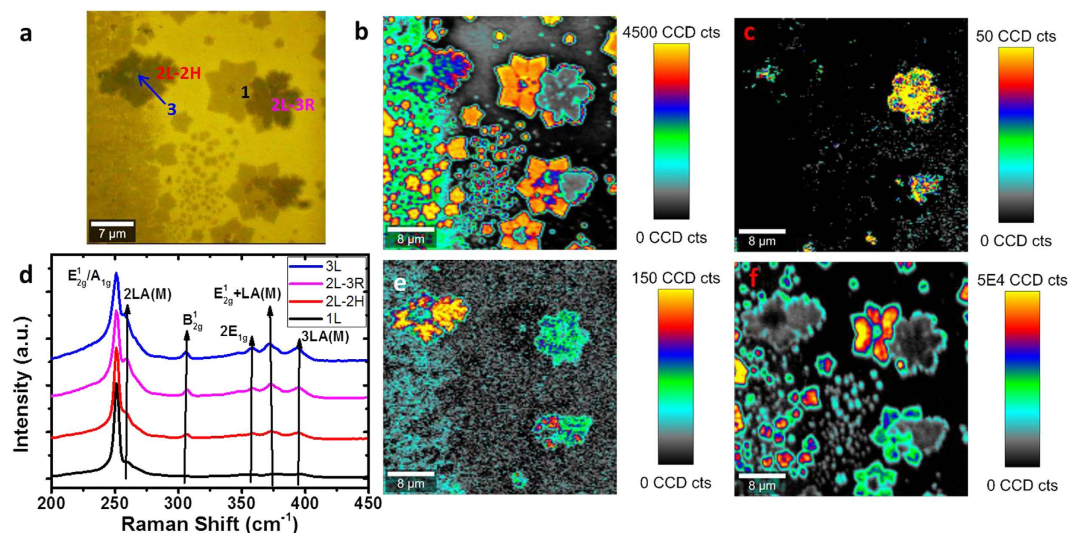


Figure 6. (a) Optical image of CVD WSe₂ with varying layer numbers. (b) Peak intensity map of A'₁/A_{1g} and E'₁/E_g/E'_{2g} overlapping modes (~250 cm⁻¹). (c) Peak intensity map of 2LA(M) peak (~260 cm⁻¹). (d) Raman spectra of 1L, 2L-2H, 2L-3R and 3L-2H WSe₂. (e) Peak intensity map of A'₁/A_{1g}/B_{2g} (~310 cm⁻¹) Raman mode. (f) PL intensity map.

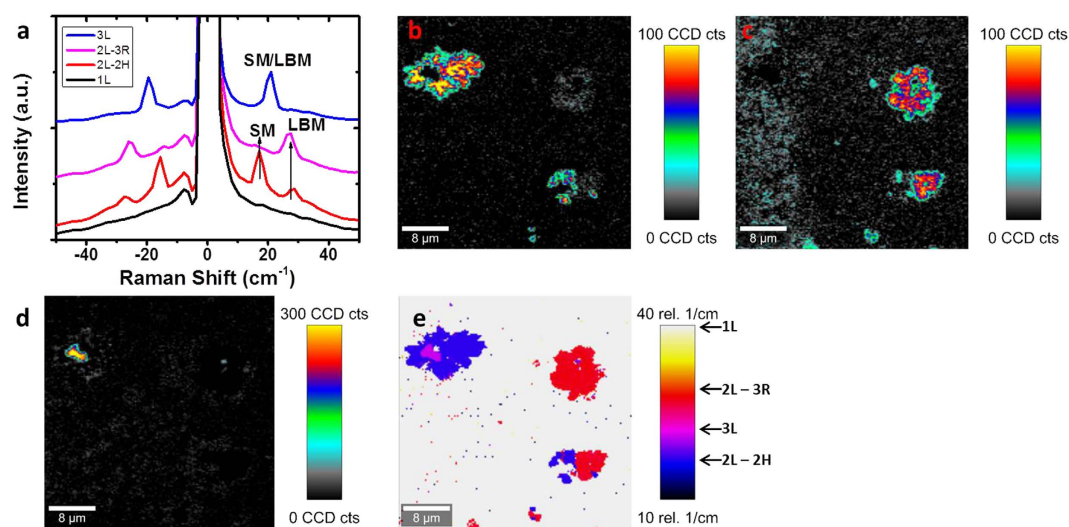


Figure 7. (a) Low-frequency Raman spectra of SMs and LBMs of 1, 2 and 3L WSe₂. (b) Peak intensity map of SM mode for 2L-2H WSe₂ at ~17 cm⁻¹. (c) Peak intensity map for 2L-3R WSe₂ at ~27 cm⁻¹. (d) Peak intensity map of SM/LBM mode for 3L-2H WSe₂ at ~21 cm⁻¹. (e) Map of position of maximum peak intensity of the low-frequency Raman modes in the range of 10–40 cm⁻¹.

intensity map is shown in Fig. 6(e), with the corresponding peak position map shown in Figure S7(d). This mode, similar to the case for MoSe₂, is inactive in bulk material, but becomes Raman active in few-layer samples⁴². However, the absence of a discernible change in the intensity or position for 2–3 layers means it is of little use for layer-number analysis. Interestingly, this mode is most intense in the case of one 2L stacking configuration, which we tentatively attribute to increased interlayer interactions in ideal (likely 2H stacking) in comparison to other (3R) configurations. The brightest areas in the PL intensity map in Fig. 6(f) signify the presence of monolayers. This is confirmed by the extracted PL spectra and position map shown in Figure S7(c) and (e), respectively in the Supporting Information. As layer number increases, the PL position shifts to higher wavelengths (lower band-gap), and decreases in intensity, as is expected due to the change in band structure^{1,63}. No significant change in PL intensity or position is seen between the two different bilayer regions.

The low-frequency Raman modes of WSe₂ are shown in Fig. 7. Figure 7(a) shows spectra of 1 to 3L WSe₂ SMs and LBMs, which have been extracted from different areas marked in the optical image in Fig. 6(a), and are in close agreement with spectra previously reported^{56,58}. A clear decrease in intensity of the SM from 2L-2H to 2L-3R stacking is observed, with a corresponding increase in the LBM. The low-frequency peaks shown here

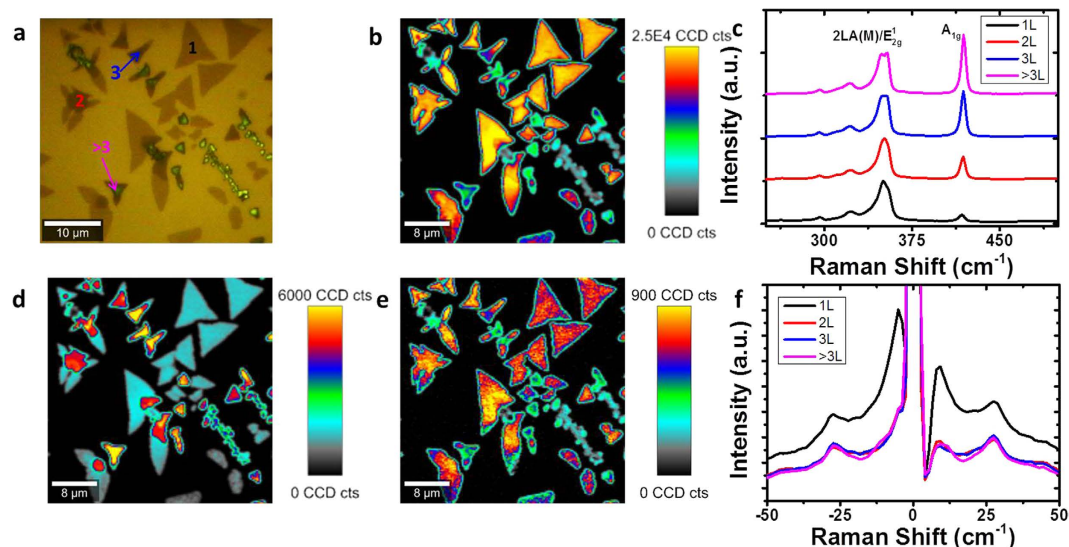


Figure 8. (a) Optical image of CVD WS₂ with varying layer numbers. (b) Peak intensity map of $2LA(M) + E'_1/E_g/E^1_{2g}$ ($\sim 352\text{ cm}^{-1}$). (c) Raman spectra of 1, 2, 3, and $>3L$ WS₂ in the high-frequency region. (d) Peak intensity map of max A'_1/A_{1g} peak ($\sim 417\text{ cm}^{-1}$). (e) Peak intensity map of low-frequency resonance mode at 27 cm^{-1} in WS₂. (f) Raman spectra of 1, 2, 3, and $4L$ WS₂ in the low-frequency region.

agree well with different stacking configurations of $2L$ WSe₂ reported previously⁵⁸. A Raman map of the $2L$ SM ($\sim 17\text{ cm}^{-1}$) intensity is shown in Fig. 7(b), which shows (with some overlap with peaks present in different layers) the areas where $2L$ - $2H$ coverage is present. This is also shown for intensity maps of $2L$ - $3R$ LBM ($\sim 27\text{ cm}^{-1}$) and $3L$ - $2H$ SM/LBM peak overlap ($\sim 21\text{ cm}^{-1}$) shown in Fig. 7(c,d), respectively. A map of the position of maximum intensity in the low-frequency region is shown in Fig. 7(e), where the measurement of peak position over the range of 10 – 40 cm^{-1} allows for some clarification of each layer from a single Raman map.

WS₂ Raman Mapping

A sample of CVD grown WS₂ with a variety of layer numbers present is shown in Fig. 8(a). The WS₂ Raman spectrum with an excitation wavelength of 532 nm is characterized by the $E'_1/E_g/E^1_{2g}$ and A'_1/A_{1g} modes at $\sim 355\text{ cm}^{-1}$ and 417 cm^{-1} , respectively, and the resonant $2LA(M)$ phonon mode at $\sim 352\text{ cm}^{-1}$, similar to that discussed previously for WSe₂. The resonance mode appears here due to the 532 nm laser wavelength used being in resonance with the B exciton peak of WS₂^{61,62,64}. Resonant Raman spectroscopy is a powerful tool in the study of exciton-phonon interactions in 2D materials; through careful selection of the excitation wavelength certain modes can be enhanced and additional resonant contributions such as the $2LA(M)$ mode observed⁶⁵. A Raman map of intensity of the peak centred at $\sim 352\text{ cm}^{-1}$ is shown in Fig. 8(b), with the corresponding peak position map in Figure S8(a) in the supporting information. This peak is a combination of contributions from the resonant $2LA(M)$ and $E'_1/E_g/E^1_{2g}$ modes that coincidentally overlap at this Raman shift. This peak is most intense in monolayer crystals, correlating to the PL map in Fig. 8(e). A Raman map of the A'_1/A_{1g} mode intensity is shown in Fig. 8(d), with the corresponding peak position map shown in Figure S8(b) in the Supporting Information. The Raman spectrum of these layers is shown in Fig. 8(c), with the spectra normalized to the peak at 352 cm^{-1} and offset for clarity. This shows changing behaviour from monolayer to few-layer crystals that is consistent with previous reports^{26,66}. The remarkable PL in WS₂ monolayers is evident in the PL intensity map and spectrum in Figure S8(e) and (g) in the Supporting Information. The apparent absence of PL in this map for $2+$ layers is simply due to the relative intensity of the PL in $2+$ layers being dwarfed by the emission from the monolayer crystals, where the intensity ratio of PL to $2LA(M)/E^1_{2g}$ is ~ 25 . Further changes in PL between mono and few-layer films are evident in the map of PL peak position in Figure S8(f) in the Supporting Information, which demonstrates the position shift from $\sim 640\text{ nm}$ for monolayers to $\sim 650\text{ nm}$ for few layers, as is expected as the addition of layers causes shifting of the band structure towards a smaller and more indirect bandgap.

While for MoS₂, MoSe₂ and WSe₂ we have highlighted the practicality of low-frequency Raman spectroscopy for assessment of layer-number and stacking orientation, in the case of WS₂ we will now discuss the possible presence of resonant modes in the low-frequency region of the Raman spectrum. Low-frequency Raman spectra of WS₂ regions of different layer thickness are shown in Fig. 8(f). We observe a peak at $\sim 27\text{ cm}^{-1}$ for all layer numbers, essentially obscuring SMs and LBMs at the Raman excitation wavelength used (532 nm). This peak is most intense in monolayer, as can be seen by the map in Fig. 8(e). A recent report has shown similar behaviour in the low-frequency region of the Raman spectrum of MoS₂ probed with a 633 nm excitation laser⁶⁷ and attributed this to strong resonance with excitons or exciton-polaritons, while previous reports have attributed this resonant Raman process to be reflective of a subtle splitting in the conduction band at K points⁶⁸. We tentatively assign this new peak in WS₂ as a $LA(M)$ related mode, due to the peak intensity maps appearing almost identical in relative intensity to the $2LA(M)$ peak intensity map shown in Fig. 8(b). It should be noted that these resonance

effects are not seen in WSe₂, with the laser wavelength used (532 nm), as this is only in resonance with the A' split exciton peak, and not an exciton absorption peak as is the case for WS₂⁶¹. This peak is seen in WS₂ for all layer thicknesses measured and while it is most intense in monolayer it does not vary significantly in intensity for other layer numbers. To further strengthen the link between this newly observed peak and the resonant modes, a comparison between Figure S8(c) in the Supporting Information, a peak intensity map of the LA(M) mode, and the low-frequency resonance peak shown here in Fig. 8(e), shows that these correlate in relative intensity. It is suggested that further exploration of WS₂ low-frequency modes with multiple wavelengths would confirm this assignment, as has held true for MoS₂^{67,68}.

Conclusion

A comprehensive study of Raman scattering in CVD-grown mono- and few-layer MoS₂, MoSe₂, WSe₂ and WS₂ has been presented. Phonon modes for in-plane and out-of-plane vibrations show thickness dependent intensities and positions in both the high- and low-frequency regions. The general peak shift trends are similar for all materials studied due to their similar lattice structures, where a stiffening (blue shift) is observed in SMs, while a softening (red shift) is observed in LBMs, with increasing layer number. However, the intensity dependencies and Raman shifts vary in each material due to the different atomic masses of the metal/chalcogen in each crystal type, and due to the stacking order of the layers. The determination of layer number via systematic low-frequency mode mapping is a crucial development in the research and analysis of TMD thin films, as is the stacking configuration determination, which we have shown here by Raman mapping techniques. We further report a new peak observable in resonance conditions at ~27 cm⁻¹ in WS₂ crystals.

In future, low-frequency Raman mapping could readily be applied to quickly assess the layer number of TMDs produced by other methods, such as liquid-phase exfoliation, to ascertain their suitability for specific applications. Importantly, this methodology could be extended to other TMD crystals that do not show significant changes in the high-frequency region of their Raman spectrum with layer number, such as ReS₂⁶⁹. Furthermore, it is anticipated that this technique will be useful for investigating layer number and stacking orientation in 2D material alloys⁷⁰ and recently fabricated TMD heterostructures^{39,40}.

Materials and Methods

CVD growth of TMDs. Precursor layers of MoO₃ (WO₃) were liquid-phase exfoliated and dispersed onto commercially available silicon dioxide (SiO₂, ~290 nm thick) substrates as described previously^{28,71}. The MoO₃ (WO₃) precursor substrates were then placed in a quartz boat with a blank 300 nm SiO₂/Si substrate face down on top of them, creating a microreactor. This was then placed in the centre of the heating zone of a quartz tube furnace, and ramped to 750 °C under 150 sccm of forming gas (10% H₂ in Ar) flow at a pressure of ~0.7 torr. Sulfide and selenide films were grown in separate, dedicated systems to avoid cross contamination.

For MSe₂ growth. Se vapour was then produced by heating Se powder to ~220 °C in an independently controlled upstream heating zone of the furnace, and carried downstream to the microreactor for a duration of 30 minutes after which the furnace was cooled down to room temperature.

For MS₂ growth. S vapour was then produced by heating S powder to ~120 °C in an independently controlled upstream heating zone of the furnace, and carried downstream to the microreactor for a duration of 20 minutes after which the furnace was held at 750 °C for 20 minutes before being cooled down to room temperature.

A schematic of the growth setup used is shown in Figure S9 in the Supporting Information. While the described growth procedure can produce large-area monolayer coverage²⁸, areas consisting of crystals with a variety of layer thicknesses were specifically chosen to highlight the capability of low-frequency Raman mapping for layer-number and stacking-orientation investigation.

Raman and PL Analysis. Raman and PL spectroscopy were performed using a Witec alpha 300R with a 532 nm excitation laser and a laser power of <500 μW, in order to minimize sample damage. The Witec alpha 300R was fitted with a Rayshield Coupler to detect Raman lines close to the Rayleigh line at 0 cm⁻¹. A spectral grating with 1800 lines/mm was used for all Raman spectra whereas a spectral grating with 600 lines/mm was used for PL measurements. The spectrometer was calibrated to a Hg/Ar calibration lamp (Ocean Optics) prior to the acquisition of spectra. Maps were generated by taking 4 spectra per μm in both x and y directions over large areas. AFM measurements were carried out using a Veeco Dimension 3100 in tapping mode, with 40 N/m probes from Budget Sensors.

References

- Mak, K. F., Lee, C., Hone, J., Shan, J. & Heinz, T. F. Atomically Thin MoS₂: A New Direct-Gap Semiconductor. *Phys Rev Lett* **105**, 136805 (2010).
- Splendiani, A. *et al.* Emerging photoluminescence in monolayer MoS₂. *Nano Lett* **10**, 1271–1275 (2010).
- Radisavljevic, B., Radenovic, A., Brivio, J., Giacometti, V. & Kis, A. Single-layer MoS₂ transistors. *Nat. Nanotechnol.* **6**, 147–150 (2011).
- Lembke, D. & Kis, A. Breakdown of High-Performance Monolayer MoS₂ Transistors. *ACS nano* **6**, 10070–10075 (2012).
- Lopez-Sanchez, O. *et al.* Light Generation and Harvesting in a van der Waals Heterostructure. *ACS Nano* **8**, 3042–3048 (2014).
- Lopez-Sanchez, O., Lembke, D., Kayci, M., Radenovic, A. & Kis, A. Ultrasensitive photodetectors based on monolayer MoS₂. *Nat. Nanotechnol.* **8**, 497–501 (2013).
- Yim, C. *et al.* Heterojunction Hybrid Devices from Vapor Phase Grown MoS₂. *Scientific reports* **4**, 5458 (2014).
- Nolan, H. *et al.* Molybdenum disulfide/pyrolytic carbon hybrid electrodes for scalable hydrogen evolution. *Nanoscale* **6**, 8185–8191 (2014).
- Acerce, M., Voiry, D. & Chhowalla, M. Metallic 1T phase MoS₂ nanosheets as supercapacitor electrode materials. *Nat Nano* **10**, 313–318 (2015).

10. Wang, T. *et al.* Size-Dependent Enhancement of Electrocatalytic Oxygen-Reduction and Hydrogen-Evolution Performance of MoS₂ Particles. *Chemistry – A European Journal* **19**, 11939–11948 (2013).
11. Eda, G. *et al.* Photoluminescence from Chemically Exfoliated MoS₂. *Nano Letters* **11**, 5111–5116 (2011).
12. Coleman, J. N. *et al.* Two-Dimensional Nanosheets Produced by Liquid Exfoliation of Layered Materials. *Science* **331**, 568–571 (2011).
13. Backes, C. *et al.* Edge and confinement effects allow *in situ* measurement of size and thickness of liquid-exfoliated nanosheets. *Nat Commun* **5**, 4576 (2014).
14. Lee, K. *et al.* Electrical Characteristics of Molybdenum Disulfide Flakes Produced by Liquid Exfoliation. *Advanced Materials* **23**, 4178–4182 (2011).
15. Nicolosi, V., Chhowalla, M., Kanatzidis, M. G., Strano, M. S. & Coleman, J. N. Liquid exfoliation of layered materials. *Science* **340**, 1226419 (2013).
16. O'Brien, M. *et al.* Plasma assisted synthesis of WS₂ for gas sensing applications. *Chemical Physics Letters* **615**, 6–10 (2014).
17. Lin, Y.-C. *et al.* Wafer-scale MoS₂ thin layers prepared by MoO₃ sulfurization. *Nanoscale* **4**, 6637–6641 (2012).
18. Lee, K., Gatensby, R., McEvoy, N., Hallam, T. & Duesberg, G. S. High-performance sensors based on molybdenum disulfide thin films. *Adv Mater* **25**, 6699–6702 (2013).
19. Kong, D. *et al.* Synthesis of MoS₂ and MoSe₂ Films with Vertically Aligned Layers. *Nano Letters* **13**, 1341–1347 (2013).
20. Gatensby, R. *et al.* Controlled synthesis of transition metal dichalcogenide thin films for electronic applications. *Appl Surf Sci* **297**, 139–146 (2014).
21. Amani, M. *et al.* Electrical performance of monolayer MoS₂ field-effect transistors prepared by chemical vapor deposition. *Appl Phys Lett* **102**, 193107 (2013).
22. Lee, Y. H. *et al.* Synthesis of large-area MoS₂ atomic layers with chemical vapor deposition. *Adv Mater* **24**, 2320–2325 (2012).
23. Zhan, Y., Liu, Z., Najmaei, S., Ajayan, P. M. & Lou, J. Large-area vapor-phase growth and characterization of MoS₂ atomic layers on a SiO₂ substrate. *Small* **8**, 966–971 (2012).
24. Néstor, P.-L. *et al.* CVD-grown monolayered MoS₂ as an effective photosensor operating at low-voltage. *2D Materials* **1**, 011004 (2014).
25. Gutiérrez, H. R. *et al.* Extraordinary Room-Temperature Photoluminescence in Triangular WS₂ Monolayers. *Nano Lett* **13**, 3447–3454 (2012).
26. Berkdemir, A. *et al.* Identification of individual and few layers of WS₂ using Raman Spectroscopy. *Scientific reports* **3**, 1755 (2013).
27. Elías, A. L. *et al.* Controlled Synthesis and Transfer of Large-Area WS₂ Sheets: From Single Layer to Few Layers. *ACS Nano* **7**, 5235–5242 (2013).
28. O'Brien, M. *et al.* Transition Metal Dichalcogenide Growth via Close Proximity Precursor Supply. *Sci. Rep.* **4**, 7374 (2014).
29. Ferrari, A. C. & Basko, D. M. Raman spectroscopy as a versatile tool for studying the properties of graphene. *Nat Nano* **8**, 235–246 (2013).
30. Zhang, X. *et al.* Raman spectroscopy of shear and layer breathing modes in multilayer MoS₂. *Phys Rev B* **87**, 115413 (2013).
31. Kappera, R. *et al.* Phase-engineered low-resistance contacts for ultrathin MoS₂ transistors. *Nature materials* **13**, 1128–1134 (2014).
32. Song, I., Park, C. & Choi, H. C. Synthesis and properties of molybdenum disulfide: from bulk to atomic layers. *RSC Advances* **5**, 7495–7514 (2015).
33. Puzos, A. A. *et al.* Low-Frequency Raman Fingerprints of Two-Dimensional Metal Dichalcogenide Layer Stacking Configurations. *ACS Nano* (2015).
34. Suzuki, R. *et al.* Valley-dependent spin polarization in bulk MoS₂ with broken inversion symmetry. *Nat. Nanotechnol.* **9**, 611–617 (2014).
35. Xia, M. *et al.* Spectroscopic Signatures of AA' and AB Stacking of Chemical Vapor Deposited Bilayer MoS₂. *ACS Nano*, doi: 10.1021/acsnano.1025b05474 (2015).
36. Geim, A. K. & Grigorieva, I. V. Van der Waals heterostructures. *Nature* **499**, 419–425 (2013).
37. Lui, C. H. *et al.* Observation of interlayer phonon modes in van der Waals heterostructures. *Phys Rev B* **91**, 165403 (2015).
38. van der Zande, A. M. *et al.* Tailoring the Electronic Structure in Bilayer Molybdenum Disulfide via Interlayer Twist. *Nano Letters* **14**, 3869–3875 (2014).
39. Withers, F. *et al.* Light-emitting diodes by band-structure engineering in van der Waals heterostructures. *Nature materials* **14**, 301–306 (2015).
40. Gong, Y. *et al.* Vertical and in-plane heterostructures from WS₂/MoS₂ monolayers. *Nature materials* **13**, 1135–1142 (2014).
41. Terrones, H. *et al.* New First Order Raman-active Modes in Few Layered Transition Metal Dichalcogenides. *Scientific reports* **4**, 4215 (2014).
42. Tonndorf, P. *et al.* Photoluminescence emission and Raman response of monolayer MoS₂, MoSe₂, and WSe₂. *Opt. Express* **21**, 4908–4916 (2013).
43. Scheuschner, N., Gillen, R., Staiger, M. & Maultzsch, J. Interlayer resonant Raman modes in few-layer MoS₂. *Phys Rev B* **91**, 235409 (2015).
44. Li, H. *et al.* From Bulk to Monolayer MoS₂: Evolution of Raman Scattering. *Advanced Functional Materials* **22**, 1385–1390 (2012).
45. Zhao, W. J. *et al.* Evolution of Electronic Structure in Atomically Thin Sheets of WS₂ and WSe₂. *ACS Nano* **7**, 791–797 (2013).
46. Lee, C. *et al.* Anomalous Lattice Vibrations of Single- and Few-Layer MoS₂. *ACS Nano* **4**, 2695–2700 (2010).
47. Xia, J. *et al.* CVD synthesis of large-area, highly crystalline MoSe₂ atomic layers on diverse substrates and application to photodetectors. *Nanoscale* **6**, 8949–8955 (2014).
48. Mignuzzi, S. *et al.* Effect of disorder on Raman scattering of single-layer MoS₂. *Phys Rev B* **91**, 195411 (2015).
49. Chakraborty, B. *et al.* Symmetry-dependent phonon renormalization in monolayer MoS₂ transistor. *Phys Rev B* **85**, 161403 (2012).
50. Shi, Y. *et al.* Selective Decoration of Au Nanoparticles on Monolayer MoS₂ Single Crystals. *Scientific reports* **3**, 1839 (2013).
51. Conley, H. *et al.* Bandgap Engineering of Strained Monolayer and Bilayer MoS₂. *Nano Letters* (2013).
52. Castellanos-Gomez, A. *et al.* Local Strain Engineering in Atomically Thin MoS₂. *Nano Letters* **13**, 5361–5366 (2013).
53. Tan, P. H. *et al.* The shear mode of multilayer graphene. *Nature materials* **11**, 294–300 (2012).
54. Zhao, Y. *et al.* Interlayer breathing and shear modes in few-trilayer MoS₂ and WSe₂. *Nano Lett* **13**, 1007–1015 (2013).
55. Lui, C. H. & Heinz, T. F. Measurement of layer breathing mode vibrations in few-layer graphene. *Phys Rev B* **87**, 121404 (2013).
56. Chen, S.-Y., Zheng, C., Fuhrer, M. S. & Yan, J. Helicity-Resolved Raman Scattering of MoS₂, MoSe₂, WS₂, and WSe₂ Atomic Layers. *Nano Letters* **15**, 2526–2532 (2015).
57. O'Brien, M. *et al.* Low wavenumber Raman spectroscopy of highly crystalline MoSe₂ grown by chemical vapor deposition. *physica status solidi (b)* **252**, 2385–2389 (2015).
58. Puzos, A. A. *et al.* Low-Frequency Raman Fingerprints of Two-Dimensional Metal Dichalcogenide Layer Stacking Configurations. *ACS Nano* **9**, 6333–6342 (2015).
59. Shmeliov, A. *et al.* Unusual Stacking Variations in Liquid-Phase Exfoliated Transition Metal Dichalcogenides. *ACS Nano* **8**, 3690–3699 (2014).
60. Lu, X. *et al.* Large-Area Synthesis of Monolayer and Few-Layer MoSe₂ Films on SiO₂ Substrates. *Nano Letters* **14**, 2419–2425 (2014).
61. Zhao, W. *et al.* Lattice dynamics in mono- and few-layer sheets of WS₂ and WSe₂. *Nanoscale* **5**, 9677–9683 (2013).
62. del Corro, E. *et al.* Excited Excitonic States in 1L, 2L, 3L, and Bulk WSe₂ Observed by Resonant Raman Spectroscopy. *ACS Nano* **8**, 9629–9635 (2014).

63. Molina-Sanchez, A. & Wirtz, L. Phonons in single-layer and few-layer MoS₂ and WS₂. *Phys Rev B* **84**, 155413 (2011).
64. Pimenta, M. A., del Corro, E., Carvalho, B. R., Fantini, C. & Malard, L. M. Comparative Study of Raman Spectroscopy in Graphene and MoS₂-type Transition Metal Dichalcogenides. *Accounts of Chemical Research* **48**, 41–47 (2015).
65. Carvalho, B. R., Malard, L. M., Alves, J. M., Fantini, C. & Pimenta, M. A. Symmetry-Dependent Exciton-Phonon Coupling in 2D and Bulk MoS₂ Observed by Resonance Raman Scattering. *Phys Rev Lett* **114**, 136403 (2015).
66. Cong, C. *et al.* Synthesis and Optical Properties of Large-Area Single-Crystalline 2D Semiconductor WS₂ Monolayer from Chemical Vapor Deposition. *Advanced Optical Materials* **2**, 131–136 (2014).
67. Lee, J.-U., Park, J., Son, Y.-W. & Cheong, H. Anomalous excitonic resonance Raman effects in few-layered MoS₂. *Nanoscale* **7**, 3229–3236 (2015).
68. Zeng, H. *et al.* Low-frequency Raman modes and electronic excitations in atomically thin MoS₂ films. *Phys Rev B* **86**, 241301 (2012).
69. Tongay, S. *et al.* Monolayer behaviour in bulk ReS₂ due to electronic and vibrational decoupling. *Nat Commun* **5**, 3252 (2014).
70. Feng, Q. *et al.* Growth of Large-Area 2D MoS₂(1-x)Se_{2x} Semiconductor Alloys. *Advanced Materials* **26**, 2648–2653 (2014).
71. Hanlon, D. *et al.* Production of Molybdenum Trioxide Nanosheets by Liquid Exfoliation and Their Application in High-Performance Supercapacitors. *Chemistry of Materials* **26**, 1751–1763 (2014).

Acknowledgements

This work is supported by the SFI under Contract No. 12/RC/2278 and PI_10/IN.1/I3030. M.O.B. acknowledges an Irish Research Council scholarship via the Enterprise Partnership Scheme, Project 201517, Award 12508. N.M. acknowledges SFI (14/TIDA/2329). D.H. and J.N.C. acknowledge the European Union Seventh Framework Programme under grant agreement n°604391 Graphene Flagship. The authors thank Christian Wirtz for illustrations as well as Riley Gatensby and Kangho Lee for assistance with CVD.

Author Contributions

N.M. conceived and designed the experiments. N.M. and M.O. synthesized materials by CVD, carried out spectroscopic measurements and analysis and wrote the paper. D.H. and J.N.C. carried out liquid-phase exfoliation of precursor nanosheets. T.H. performed AFM measurements. N.M. and G.S.D. supervised the whole project. All authors contributed to the discussion of the results and improvement of the manuscript.

Additional Information

Supplementary information accompanies this paper at <http://www.nature.com/srep>

Competing financial interests: The authors declare no competing financial interests.

How to cite this article: O'Brien, M. *et al.* Mapping of Low-Frequency Raman Modes in CVD-Grown Transition Metal Dichalcogenides: Layer Number, Stacking Orientation and Resonant Effects. *Sci. Rep.* **6**, 19476; doi: 10.1038/srep19476 (2016).



This work is licensed under a Creative Commons Attribution 4.0 International License. The images or other third party material in this article are included in the article's Creative Commons license, unless indicated otherwise in the credit line; if the material is not included under the Creative Commons license, users will need to obtain permission from the license holder to reproduce the material. To view a copy of this license, visit <http://creativecommons.org/licenses/by/4.0/>